Interferometric speckle visibility spectroscopy (ISVS) for human cerebral blood flow monitoring

Jian Xu,[1, a)] Ali K. Jahromi,[1, a)] Joshua Brake,[1, a)] J. Elliott Robinson,[2] and Changhuei Yang[1, b)]
[1)]*Department of Electrical Engineering, California Institute of Technology*
[2)]*Division of Biology and Biological Engineering, California Institute of Technology*

(Dated: 7 November 2020)

[a)]These authors contributed equally to this work.
[b)]Electronic mail: chyang@caltech.edu.

I. SUPPLEMENTARY NOTE

A. Optical setup

The optical setup of the ISVS system is shown in Supplementary FIG. 2. The beam from the laser (CrystaLaser, CL671-150) is split into a reference beam and a sample beam by a polarized beam splitter. The reference beam is coupled into a single mode fiber (FB1, Thorlabs, PM460-HP) for spatial filtering. The filtered beam is collimated by a single lens (L1) and illuminates on the camera (Phantom S640). The sample beam is coupled into a multimode fiber (FB2, Thorlabs M31L02) and the output beam is collimated and illuminates on the forehead of the human subject. The diffused light from the human subject is collected by a large core multimode fiber (Thorlabs M107L02). The output light field of the large core fiber is relayed onto the camera by a 4-f system (L2 and L3). A beam splitter (BS2) combines the reference beam and sample beam. A custom designed aperture (AP) is put on the Fourier plane of the 4-f system. A polarizer (P) is put in the sample arm to filter out the cross-polarization portion of the diffused light. To record the scattered light from the sample using conventional DCS methods, a beam splitter (BS1) is added in front of BS2 and an SPCM (PerkinElmer, SPCM-AQRH-14) records the scattered light intensity.

B. System implementation on rat experiments

In the dorsal skin flap blood flow monitoring experiments, isoflurane (1-5%) administered in an induction box followed by maintenance on a nose cone was used to induce anesthesia on a regular laboratory rat. The dorsal skin flap of the rat was shaved and clipped on a glass slide. The rat was put on a 3-D translational stage and the illumination beam illuminated the dorsal skin flap. A 4-f system (L2 and L3, Supplementary FIG. 2B) in the optical setup imaged the skin that diffused light.

In the dorsal skin flap blood flow monitoring experiments, ketamine 80-100 mg/kg and xylazine 8-10 mg/kg given via the intraperitoneal route was used to anesthetize a regular laboratory rat. The skin on the head and the scalp on top of the skull were surgically removed. The rat was put on a 3-D translational stage and the bregma and lambda areas were identified and illuminated by a collimated beam. A 4-f system (L2 and L3, Supplementary FIG. 2B) in the optical setup imaged the part of skull that diffused light. The distance between the illumination spot and the imaging field of view was set about 1 cm.

C. Fourier plane aperture design

To maximize the bandwidth of the signal in the spatial frequency domain, we specifically designed the shape of the aperture on the Fourier plane of the light collection 4-f system (L2 and L3, Supplementary FIG. 2A). This rectangular shape (shown in Supplementary FIG. 4A) is different from conventional circular aperture shapes (shown in Supplementary FIG. 4B), since here we cared primarily about collecting the maximum number of speckles rather than isotropic resolution in conventional imaging. The lateral size of the aperture was designed to avoid aliasing when performing off-axis holography.

D. The mathematical derivation of equivalent visibility factor

In this section, we derive the second moment of the interference term $S(\mathbf{r})$ in Supplementary Eq. 4 in the main text. Previous work from[1] has shown similar theoretical derivation as shown below, where they analyzed the interferometric detection for dynamic speckles in ultrasound modulated optical tomography.

$$
\begin{aligned}
&\langle |S(\mathbf{r})|^2 \rangle = \langle S(\mathbf{r}) \times S^*(\mathbf{r}) \rangle \\
&= \frac{1}{T} \left\langle \int_0^T |E_\mathrm{R}||E_\mathrm{S}(\mathbf{r},t_1)| e^{i\phi_\mathrm{S}(\mathbf{r},t_1)} dt_1 \times \int_0^T |E_\mathrm{R}||E_\mathrm{S}(\mathbf{r},t_1)| e^{-i\phi_\mathrm{S}(\mathbf{r},t_1)} \right\rangle dt_1 \\
&= \frac{I_R}{T^2} \int_0^T \int_0^T dt_1 dt_2 \big\langle |E_\mathrm{S}(\mathbf{r},t_1)| e^{i\phi_\mathrm{S}(\mathbf{r},t_1)} |E_\mathrm{S}(\mathbf{r},t_2)| e^{-i\phi_\mathrm{S}(\mathbf{r},t_2)} \big\rangle \\
&= \frac{I_R}{T^2} \int_0^T \int_0^T dt_1 dt_2 \big\langle E_\mathrm{S}(\mathbf{r},t_1) E_\mathrm{S}^*(\mathbf{r},t_2) \big\rangle \\
&= \frac{I_R \bar{I_S}}{T^2} \int_0^T \int_0^T dt_1 dt_2 \; g_1(t_1 - t_2).
\end{aligned} \tag{1}
$$

Here $g_1(t)$ is the field decorrelation function. Change the integration variable by $\begin{cases} t = t_1 \\ \tau = t_1 - t_2 \end{cases}$, the integration in Supplementary Eq. 1 can be written as

$$\begin{aligned}
&\int_0^T \int_0^T dt_1 dt_2 g_1(t_1 - t_2) = \int_0^T \int_{-t}^{t} d\tau g_1(\tau) \\
&= \int_0^T \int_{\tau}^{T} dt g_1(\tau) + \int_{-T}^{0} \int_{-\tau}^{T} dt g_1(\tau) \\
&= \int_0^T 2(1 - \frac{\tau}{T}) g_1(\tau) d\tau = \int_0^T 2(1 - \frac{t}{T}) g_1(t) dt
\end{aligned} \tag{2}$$

given $g_1(t)$ is symmetric. Therefore, Supplementary Eq. 2 can be reduced to

$$\langle |S(\mathbf{r})|^2 \rangle = \frac{I_R \bar{I_S}}{T^2} \int_0^T 2(1 - \frac{t}{T}) g_1(t) dt. \tag{3}$$

The equivalent visibility factor is defined as $F = \frac{\langle |S(\mathbf{r})|^2 \rangle}{I_R \bar{I_S}} = \frac{1}{T} \int_0^T 2(1 - \frac{t}{T}) g_1(t)$ (shown in Eq. 5 in the main text). The definition of equivalent visibility factor and the conventional SVS visibility factor (Eq. 8 in Ref. 2) have very similar forms, while the only difference within the integral is that $g_1(t)$ in ISVS equivalent visibility factor does not have square. In fact, in Eq. 8 in Ref. 2, the $g_1(t)^2$ comes from the Siegert relation that relates the intensity correlation and field correlation. In our case, the interferometric detection directly accesses the complex field, and the Siegert relation is not needed. Therefore, when we do correlation operation on the complex field, we can get the correlation function $g_1(t)$ directly, as shown in Supplementary Eq. 1.

If $g_1(t)$ has a form of $g_1(t) = e^{-t/\tau}$ where τ is the speckle decorrelation time, after substituting in Supplementary Eq. 3, we can get

$$F = \frac{\langle |S(\mathbf{r})|^2 \rangle}{I_R \bar{I_S}} = \frac{2\tau}{T} [1 + \frac{\tau}{T} (e^{-T/\tau} - 1)]. \tag{4}$$

As $\tau \ll T$, $\tau/T \ll 1$ and the equivalent visibility factor F converges to $2\tau/T$.

In real cases, the equivalent visibility factor calculated from Supplementary Eq. 4 has a non-zero offset. Even when no signal light photons hit the camera, there is still spatial fluctuations in the cropped side lobes due to camera noise. Taking square and summing up all the pixels give a non-zero offset that is related to camera noise. Therefore, in the main text FIG. 2B, we use a camera noise corrected model to describe the equivalent visibility factor.

$$F = (1 - \beta) + \beta \frac{2\tau}{T} [1 + \frac{\tau}{T} (e^{-T/\tau} - 1)] \tag{5}$$

In Supplementary Eq. 5, a correction factor β is introduced to compensate the noise associated non-zero offset of F when T/τ is large. Ideally, β should be 1. The experimental data in the main text FIG. 2B is fitted by the expression of Supplementary Eq. 5 with β equal 0.75.

In Supplementary FIG. 6, we show a figure of equivalent visibility factor F versus T/τ with different β's. A small β implies a relatively large camera noise, therefore the offset of F, which is $F = 1 - \beta$, is higher.

II. SUPPLEMENTARY FIGURES

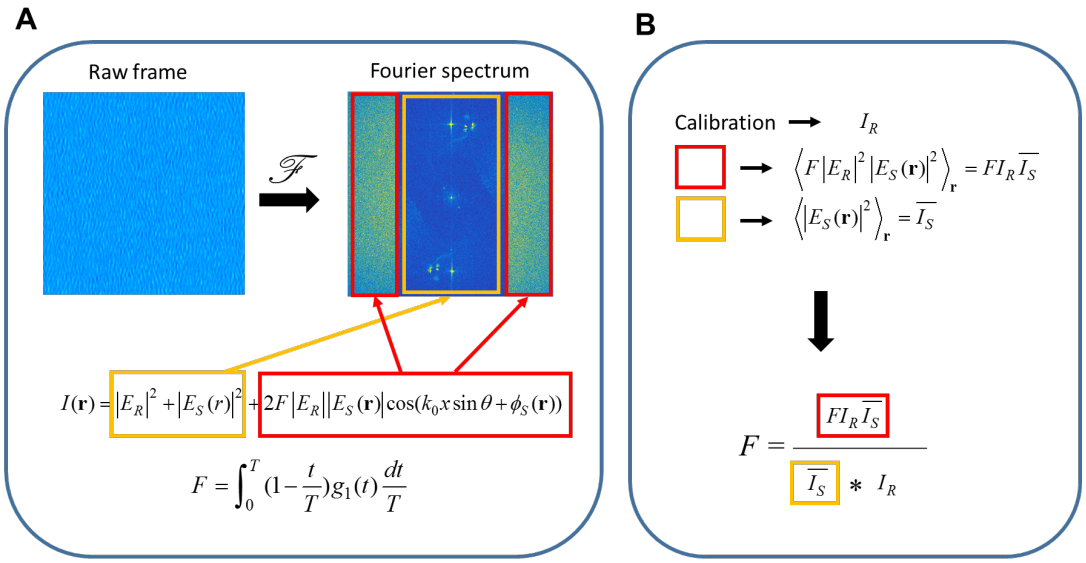

FIG. 1. Flowchart of data processing. (A) The raw frame is Fourier transformed and three lobes contain the information of the reference beam and sample beam. The yellow enclosed circle and rectangle contain the intensity information of the reference beam and sample beam, and the red enclosed circle and rectangle contain the information of the equivalent visibility factor and the complex fields. (B) The reference beam calibration provides the mean value of the reference beam intensity, the red enclosed rectangle in (A) provides the mean value of the energy in one of the interference lobes, and the yellow enclosed rectangle in (A) provides the mean value of the sample beam intensity after subtracting the reference beam mean intensity. $< \cdot >$ denotes the ensemble average over space.

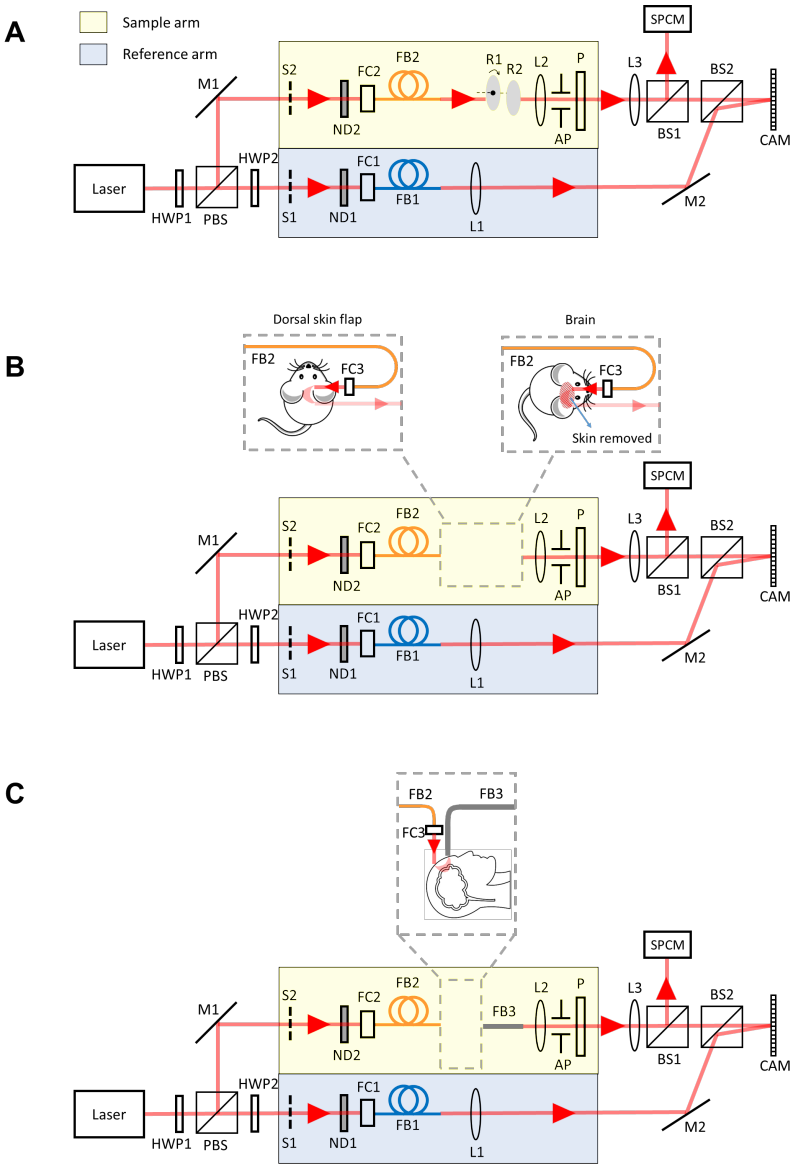

FIG. 2. Schematic of the optical setup. (A) Optical setup for diffuser experiments. (B) Optical setup for animal experiments. (C) Optical setup for human experiments. AP, aperture; BS, beam splitter; CAM, camera; FB, fiber; FC, fiber coupler; HWP, half-wave plate; L, lens; M, mirror; ND, neutral-density filter; P, polarizer; R, rotating diffuser; SPCM, single photon counting module.

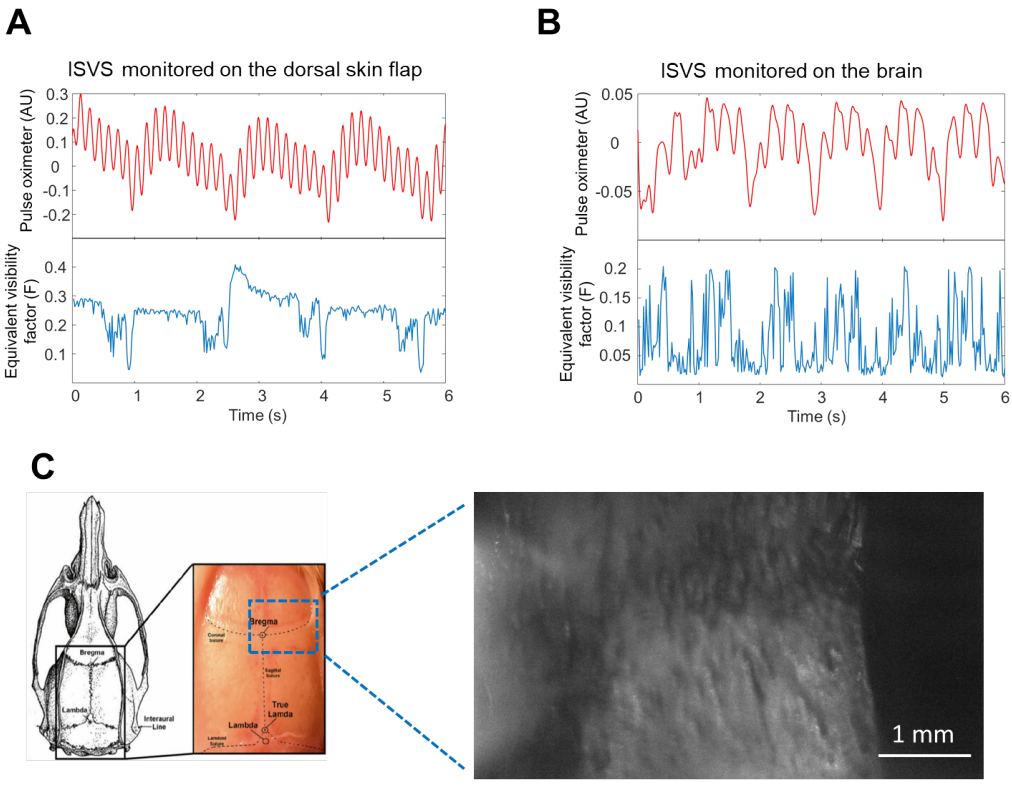

FIG. 3. Results of rat experiments. (A) The results clearly show the breathing signal at 1.5 Hz from both the pulse oximeter and ISVS equivalent visibility factor signals (four big dips). Pulsatile signals at 3.5 Hz are shown in the pulse oximeter but not clearly shown in ISVS from the dorsal skin flap. This might be due to less arterial vessels in dorsal skin flap as well as the process of clipping the skin. (B) The results show the breathing signal at 1.0 Hz from both the pulse oximeter and ISVS equivalent visibility factor signals. Pulsatile blood flow signals in ISVS couple with the breathing signals in brain signal measurements. (C) The wide field image of the brain bregma area of the rat using white LED illumination. The pulse oximeter in both measurements samples at 1 kHz. The camera frame rate in the ISVS system in both measurements is set at 50 Hz and the exposure time is set as 16 ms. The left panel is adapted from Ref. 3.

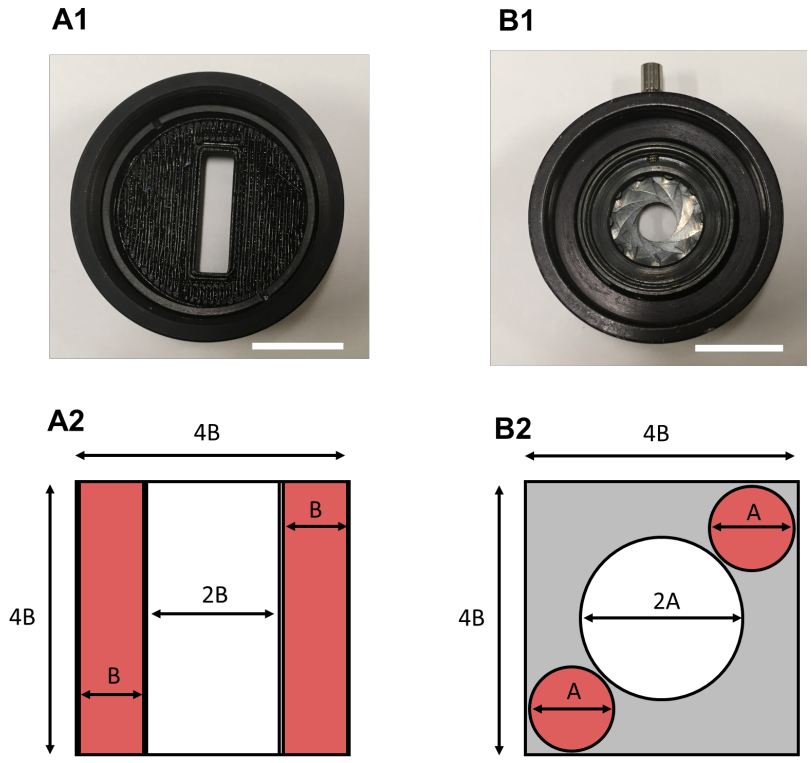

FIG. 4. Fourier plane aperture design. (A1) Rectangular aperture. (A2) The Fourier spectrum of an off-axis hologram with a rectangular aperture. (B1) Circular aperture. (B2) The Fourier spectrum of an off-axis hologram with a circular aperture. Mathematically, it can be shown that $A = \frac{4\sqrt{2}}{3+\sqrt{2}}B \approx 1.28B$. Therefore, the circular aperture uses $\frac{2\pi A^2/4}{(4B)^2} \approx 16\%$ (red circles in (B2) of the Fourier space while the rectangular aperture uses 50% (red rectangles in (A2)) of the Fourier space. The larger area in Fourier space allows higher light collection efficiency. Scale bar, 1 cm.

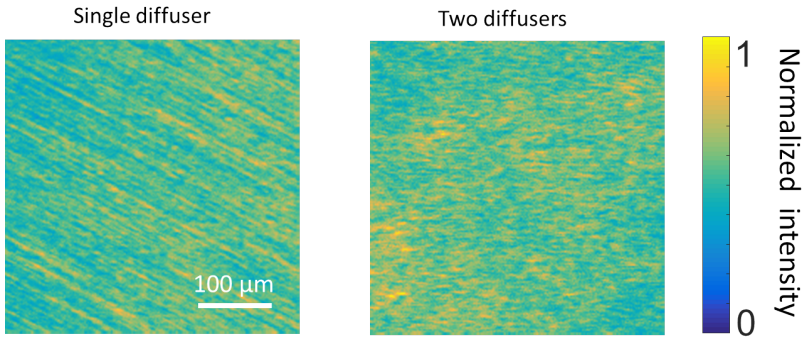

FIG. 5. Examples of dynamic speckle patterns realized by a single rotating diffuser and two diffusers (one static and one rotating). A series of translating speckle patterns realized by a single rotating diffuser result in the "smear" effect, while the use of one static and one rotating avoids such effect.

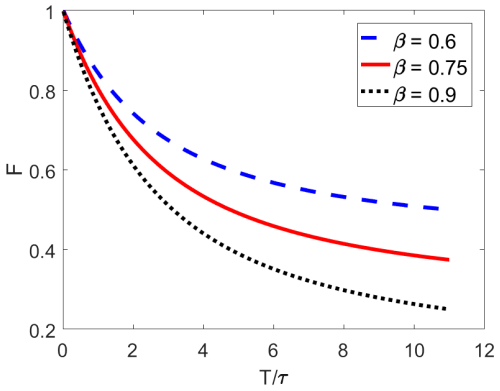

FIG. 6. Equivalent visibility factor F versus T/τ with different β's.

REFERENCES

[1]A. Hussain, W. Steenbergen, and I. M. Vellekoop, "Imaging blood flow inside highly scattering media using ultrasound modulated optical tomography," J. Biophotonics **11**, 1 (2018).

[2]R. Bandyopadhyay, A. S. Gittings, S. S. Suh, P. K. Dixon, and D. J. Durian, "Speckle-visibility spectroscopy: A tool to study time-varying dynamics," Rev. Sci. Instrum. **76**, 93110 (2005).

[3]M. J. Benskey and F. P. Manfredsson, "Intraparenchymal stereotaxic delivery of rAAV and special considerations in vector handling," in *Gene Therapy for Neurological Disorders* (Springer New York, 2016) pp. 199–215.